

## Enhancing Dental Ceramic Prostheses with Zirconia Nanocomposites: An In-Vitro Study on Hard Tissue Rehabilitation



Mohammed Hammed\*<sup>ORCID</sup>, Manal Abbood, Sadeer Majeed

Division of Medical and Industrial Materials Science, Department of Applied Sciences, University of Technology, Baghdad 10066, Iraq

Corresponding Author Email: [mohammed.m.hammed1996@gmail.com](mailto:mohammed.m.hammed1996@gmail.com)

Copyright: ©2024 The authors. This article is published by IIETA and is licensed under the CC BY 4.0 license (<http://creativecommons.org/licenses/by/4.0/>).

<https://doi.org/10.18280/acsm.480201>

### ABSTRACT

**Received:** 15 December 2023

**Revised:** 12 March 2024

**Accepted:** 30 March 2024

**Available online:** 30 April 2024

#### Keywords:

*biomaterial, nano composites, nanostructures, zinc oxide NPs, silica nanoparticles, dental prostheses*

Researchers and clinicians have directed most efforts towards rehabilitating partially or completely edentulous patients to provide them with functionality and self-esteem. The objective of this work was to create two distinct kinds of nano composites employing two different kinds of polycrystalline zirconia reinforcing materials. First strengthened using sol-gel-synthesized zinc oxide nanoparticles. Secondly, precipitated amorphous silica nanoparticles. To develop the composite material, (3 mol.  $Y_2O_3$ ) was mixed with zirconia to stabilize it in the tetragonal phase with homogeneous distribution, The ZnO NPs and  $SiO_2$  NPs were then added in varied weight rates. To yield 3 mol.  $Y_2O_3$ -ZrO<sub>2</sub>-ZnONPs and 3 mol.  $Y_2O_3$ -ZrO<sub>2</sub>- $SiO_2$ NPs nano composites samples of 10 mm diameter, uniaxial pressing was applied in a metal-die cylinder at a pressure of 5 tons. The obtained samples were then sintered in air in an electrically controlled furnace for 2 hrs at a temperature of 1400°C, while the heating and cooling rates were 5°C/min. Density, porosity, and Vickers micro hardness were used to evaluate the physical and mechanical properties of the obtained samples. XRD and FE-SEM were applied to analyze the produced samples. The results showed that there was an increase in micro hardness recorded for both reinforcement groups after applying zinc oxide NPs and silica NPs. Further improvement in densification can also be emphasized. Our study demonstrates that using nanotechnology to improve clinical performance represents a potential strategy and promising approach to enhance all-ceramic restorations.

## 1. INTRODUCTION

The field of science has recently paid close attention to studies on nanoparticles because of their size-dependently attractive properties at the nano scale [1, 2]. The design, evaluation, production, and use of materials, devices, and systems at the nano scale level (1–100 nm) constitute the cutting-edge fields of science known as nanotechnology [3]. Nanotechnology is an outstanding representation of new science, as it provides designed nanomaterials with the possibility to produce materials with much better effectiveness [4]. Nano dentistry is a new branch of dentistry that uses nanostructured materials for pain relief, the diagnosis, treatment, and prevention of oral and dental illnesses, as well as for maintaining and enhancing dental health [5]. The use of nanotechnology to manufacture dental materials with improved features and antibacterial properties is a revolutionary concept [6]. Nanostructures with medical and cosmetic applications in dental implants and maxillofacial surgery are also known to accelerate the healing process and enhance skeletal integrity. Medical nanomaterials are also used in the manufacture of toothpaste to reduce sensitivity. Despite the importance of medical Nano applications, there are some potential drawbacks to their use, such as the toxic

properties of some Nano composites, such as carbon nanotubes, which have a toxic effect on cells, which can cause an increase in oxidative stress and gene-toxicity. In addition, the development of resistance to nanomaterial's as antimicrobial agents is a source of concern [7].

Dental products in the cavity of the mouth are subjected to exceptionally significant mechanical loading stresses, in addition to the complicated and constantly changing biological nature found in the oral media [8]. Ceramics are the most often utilized materials in the sector of restorative dentistry due to their aesthetically pleasing excellence and biocompatibility [9]. Ceramics fused to metal served as the preferred restorative material for tooth-and implant-supported fixed restorations in the past [10]. Then all-ceramic restorations were created as a result of efforts to enhance the aesthetic qualities of these materials, either by using a single monolithic block or a ceramic core and veneer. Feldspathic porcelain was the first to be developed, and while it has good aesthetic qualities due to the high amount of vitreous phase in its structure, it can occasionally be mechanically unreliable [11]. Industry has experienced a wide range of materials applied for ceramic restoration purposes; however, zirconia is mostly favorable [12, 13], mainly due to the high capacity of transformation toughening which assists in preventing cracks development

through the improvement of material capability of resisting localized fracture. It naturally occurs in three arrangements based on temperature; these are the monoclinic (at 25-1170°C), tetragonal (at 1170-2370°C), and cubic (at 2370°C-melting point) [14, 15]. At room temperature, Zirconia in t-form offers the best mechanical characteristics of the three forms, while stabilized oxides, for example, CaO, MgO, and Y<sub>2</sub>O<sub>3</sub>, are utilized to stabilize it in this form [12, 16]. According to several studies, Zirconia is more difficult to attach to tooth tissues than ceramic materials based on silica [17, 18]. This is because zirconia, unlike materials made of glass, has a polycrystalline structure that makes it very resistant to various surface treatments [19]. In addition, one primary problems with zirconia are that it is opacity and the unnatural white tint [20].

Recently, zinc oxide become a viable alternative and is frequently combined with other biomaterials to provide a variety of benefits, including corrosion resistance, cytocompatibility, and antimicrobial properties [21, 22]. ZnO possesses the most extensive family of nanostructures of any material, both in terms of structure and characteristics. Numerous ZnO nanostructures with various morphologies, including nano rods, nanotubes, and nano spheres, have been discovered [23]. Three different ZnO crystalline structures have been identified: "hexagonal wurtzite", "cubic zinc-blende" and the infrequently seen "cubic rock-salt" structure. Under normal circumstances, the wurtzite structure has the highest thermodynamic stability. The zinc blend is meta-stable. Despite the fact that cubic rock-salt is often only stable at very high pressures (2 GPa) [24]. Furthermore, the second-biggest application of zinc oxide is in ceramic materials [25]. In an effort to limit the possibility of dental implants failing and enhance the osteointegration process, chemical adjustments have been performed on the surfaces of dental implants with antimicrobials (ZnO NPs). After 5 and 10 days of covering the implant outer layer surface using ZnO NPs, the underneath osteoblast cells exhibited increased "proliferation", They also had antibacterial effects against *Staphylococcus aureus*. These features are beneficial in promoting the growth of bone and preventing infection at the implant location [26]. It was discovered that ZnO NPs included in toothpaste caused dentinal tubule blockage. These can also be used as stabilizers in toothpaste because they not only prevent dentin from demineralizing but also have stronger antimicrobial effects [27].

According to studies, dentin treated with ZnO NPs has a higher capacity to cause dentinal tubule occlusion, making it a useful treatment for dentinal hypersensitivity [28]. Dentin treated with ZnO NPs had higher amounts of proteoglycans, which serve as bonding (adhesive) agents that exist between the hydroxyapatite crystals and the "collagen network", enhancing dentine-mineralization [29]. According to evidence, doping is an effective approach for enhancing the physicochemical characteristics of zinc oxide [30, 31]. Doping zinc oxide enhances stability toward dissolution and improves the surface area-to-volume ratio [32].

Similarly, industrial developments in certain areas, i.e. biomedicine [33, 34], fillers [35], catalyzers [36], and drug delivery systems [37], have led silica nanoparticles to be progressively demanded over the last decade. Silica, in general, can be found in two main groups, "crystalline silica" and "amorphous silica", the arrangement of their atoms is what distinguishes crystalline silica from amorphous silica [38]. Although both versions have the same chemical formula [39].

In terms of toxicity, crystalline silica NPs are more toxic than the amorphous type, because of the more pronounced rupture of organelle membranes and higher production of ROS [40]. Amorphous SiO<sub>2</sub> is viewed as a very attractive possibility for gene carriers and imaging of molecules [41, 42].

In addition, silica nanoparticles have unique benefits, including a considerable surface area and biological compatibility [43], large cargo loading capacity, and adjustable pore size [44]. Besides, it has been employed in implants, catheters [45], and dietary supplements [46]. In particular, to our knowledge, no study has considered the incorporation of ZnO NPs with the 3Y-TZP system. Moreover, in order to rectify the problem of opacity and the unnatural white tint and produce highly aesthetic ceramic restoratives to match the surrounding natural teeth, besides overcoming the difficulty of zirconia attaching to tooth tissues, silica nanoparticles were introduced as reinforcement materials in polycrystalline zirconia. Therefore, in the current study, 3Y-TZP-ZnONPs and 3Y-TZP-SiO<sub>2</sub>NPs are synthesized and analyzed in an effort to produce and enhance the activity of composite restorative materials without degrading their physical and mechanical properties, biocompatibility, or aesthetics.

## 2. MATERIALS AND METHODS

### 2.1 Materials

The primary material chosen to manufacture the specimens was a zirconium dioxide powder (99% purity), with a particle size of 80-100 μm, purchased from Shanghai Company, China. Yttrium dioxide purchased from Chem Supply, Australia, was employed as a stabilizing agent. Zinc acetate was purchased from Advent, Navi Mumbai, India. Sodium hydroxide (NaOH), obtained from BDH, England. Silicon dioxide nano powder (precipitated Silica) with high purity and particle size of 20-30nm was purchased from Hongwa international group, China. PVA (Mw: Approx. 115,000 Dalton) was purchased from Loba Chemicals Pvt. Ltd. Mumbai, India. The media and reagents for antibacterial applications were: Mueller-Hinton Agar medium, obtained from Accumix, Spain. Ethanol, obtained from Duksan, Korea. Deionized water, obtained from Pioneer Company, Korea. Nutrient broth, obtained from Oxoid, United Kingdom. Phosphate-buffered saline, obtained from OXOID (England). Crystal violet (CV) provided by Sigma Aldrich (USA).

### 2.2 Preparation of zinc oxide nanoparticles via the Sol-Gel method



**Figure 1.** Trial timeline for preparation of ZnO nanoparticles

The ZnO NPs were synthesized chemically using a liquid phase, as previously described [47]. Zinc acetate [Zn(CH<sub>3</sub>CO<sub>2</sub>)<sub>2</sub>·2H<sub>2</sub>O] was employed as an initial material, with sodium hydroxide [NaOH] as a solvent agent. Zinc acetate was dissolved in sodium hydroxide at a molar ratio of (1:85). Shortly after continuously stirring the resultant solution for 4 hrs between 70 and 75°C, Whatman filter paper was then used for filtering. At the time of filtration, the solution was washed several times with ethanol to remove contaminants and impurities. The product that resulted was heated in an oven at 90°C for two hours before being ground. As shown in Figure 1.

### 2.3 Preparation of polyvinyl alcohol solution (The binder agent)

For the preparation of a clear PVA solution, distilled water (100mL) was used to dissolve 3g of poly vinyl alcohol. The process lasted for 2 hrs in a magnetic stirrer.

### 2.4 Preparation of (pure-Y<sub>2</sub>O<sub>3</sub>-ZrO<sub>2</sub>) nano composite specimen

To stabilize the pure composite material in the tetragonal phase, zirconium dioxide was mixed with 3 mol. Y<sub>2</sub>O<sub>3</sub> and the compact powder contained a binder of PVA (2% of the composite). Figure 2 shows a pure nano composite sample of 10mm diameter. Uniaxial pressing was applied in a metal-die cylinder at a pressure of 5 tons. The obtained model was then sintered in the air in an electrically controlled furnace (Nabertherm, p310, Germany) for two hours at 1400°C, while the rates of heating and cooling were 5°C/minute.

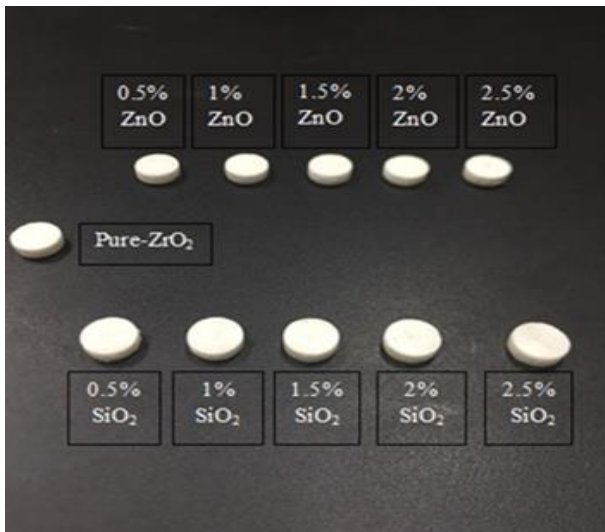


**Figure 2.** Digital image for synthesized samples

Note: The pure sample is in the exact middle. Upper line samples with zinc oxide NPs at five different weight percentage concentrations. In the lower line, there are five different weight percentages of silicon dioxide NPs

### 2.5 Preparation of (Y<sub>2</sub>O<sub>3</sub>-ZrO<sub>2</sub>-ZnO NPs) and (Y<sub>2</sub>O<sub>3</sub>-ZrO<sub>2</sub>-SiO<sub>2</sub> NPs) nano composite specimens

In order to prepare the composite material, 3 mol. Y<sub>2</sub>O<sub>3</sub> was mixed with zirconia to stable it in the tetragonal phase with homogenous distribution, where the compact powder contained a binder of PVA (2% of the composite), while the reinforcement was achieved using varied weight rates (0.5%, 1%, 1.5%, 2%, and 2.5%) wt % of ZnO NPs and SiO<sub>2</sub> NPs. To

yield 3 mol. Y<sub>2</sub>O<sub>3</sub>-ZrO<sub>2</sub>-ZnO NPs, 3 mol. Y<sub>2</sub>O<sub>3</sub>-ZrO<sub>2</sub>-SiO<sub>2</sub>NPs, nanocomposites samples of 10mm diameter, uniaxial pressing was applied in a metal-die cylinder at a pressure of 5 tons, as shown in Figure 2. The obtained models were then sintered in the air in an electrically controlled furnace (Nabertherm-p310-Germany) under the same experimental condition (2 hrs at 1400°C), with the heating and cooling rate of 5°C/minute. For all samples, compositions of all specimens are shown in the Table 1.

**Table 1.** The fundamental chemical composition of the bio-ceramic materials utilized

No.	Specimen Code	Basic Chemical Composition
1	A	(3) mol. Y <sub>2</sub> O <sub>3</sub> +ZrO <sub>2</sub>
2	B1	(3) mol. Y <sub>2</sub> O <sub>3</sub> +ZrO <sub>2</sub> +0.5wt.% ZnONPs
3	C1	(3) mol. Y <sub>2</sub> O <sub>3</sub> +ZrO <sub>2</sub> +1wt.% ZnONPs
4	D1	(3) mol. Y <sub>2</sub> O <sub>3</sub> +ZrO <sub>2</sub> +1.5wt.% ZnONPs
5	E1	(3) mol. Y <sub>2</sub> O <sub>3</sub> +ZrO <sub>2</sub> +2wt.% ZnONPs
6	F1	(3) mol. Y <sub>2</sub> O <sub>3</sub> +ZrO <sub>2</sub> +2.5wt.% ZnONPs
7	B2	(3) mol. Y <sub>2</sub> O <sub>3</sub> +ZrO <sub>2</sub> +0.5wt.% SiO <sub>2</sub> NPs
8	C2	(3) mol. Y <sub>2</sub> O <sub>3</sub> +ZrO <sub>2</sub> +1wt.% SiO <sub>2</sub> NPs
9	D2	(3) mol. Y <sub>2</sub> O <sub>3</sub> +ZrO <sub>2</sub> +1.5wt.% SiO <sub>2</sub> NPs
10	E2	(3) mol. Y <sub>2</sub> O <sub>3</sub> +ZrO <sub>2</sub> +2wt.% SiO <sub>2</sub> NPs
11	F2	(3) mol. Y <sub>2</sub> O <sub>3</sub> +ZrO <sub>2</sub> +2.5wt.% SiO <sub>2</sub> NPs

### 2.6 The procedure of measurements bulk density, apparent porosity

By applying the "Archimedes method" that utilizes distilled water, it is possible to determine the (B.D (g/cm<sup>3</sup>), A.P%) of a material in its solid state. Density can be calculated by dividing the solid's mass in the air by its weight reduction (i.e. buoyancy), following its suspension in a liquid medium to achieve the targeted weight. Measurement was made according to the international standard method, as shown in Table 2, using the following formula as Eqs. (1) and (2), while a density-measuring device was (RADWAG, manufactured in Poland):

$$B.D = \rho_L \frac{w_1}{w_3 - w_2} \quad (1)$$

B.D: Specimen's bulk density.

$\rho_L$ : Density of the liquid (for water equal to 1g/cm<sup>3</sup>).

W<sub>1</sub>: Dry specimen's weight.

W<sub>2</sub>: Soaked, immersed specimen's weight.

W<sub>3</sub>: Saturated specimen's weight.

$$A.P\% = \frac{w_3 - w_1}{w_3 - w_2} \times 100\% \quad (2)$$

A.P: Specimen's apparent porosity.

**Table 2.** Standard specifications

Specifications Standard	Specimen's Dimensions	Test Type
ASTM C373-88	Disc (10mm diameter) - (4mm thickness)	Bulk density
ASTM C373-88	Disc (10mm diameter) - (4mm thickness)	Apparent porosity
ASTM C1327-99	Disc (10mm diameter) - (4mm thickness)	Hardness

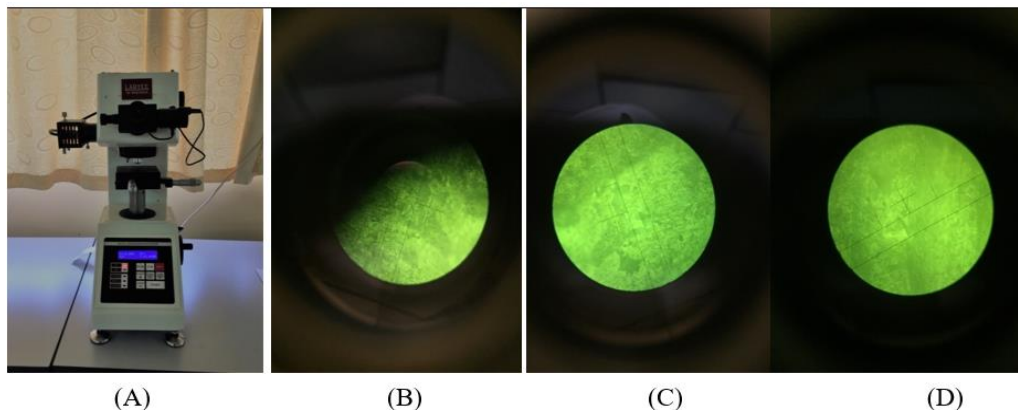


**Figure 3.** (A) Vickers microhardness test; (B, C and D) Digital image of diamond indenter with a square base for (B) Pure-3Y-TZP; (C) 3Y-TZP-ZnO NPs; (D) 3Y-TZP-SiO<sub>2</sub>NPs

## 2.7 Vickers indentation test for hardness

A Vickers indenter, which comprises a diamond pyramid, was used for hardness determination utilizing a digital micro Vickers hardness tester, manufactured in China. The hardness measurements were carried out at a constant load of 9.8 N applied for 15 seconds. The testing procedure was accomplished as specified by ASTM with the international standard method, as shown in Table 2. Samples were marked with three points, one at the center and the other two away in each direction around the central point. For each specimen, three measurements were made and the average was determined. The Vickers microhardness test was done using an optical microscope. Using a diamond indenter with a square base and a 136° included angle between the opposing faces, as shown in Figure 3. The indenter should be applied on a smooth flat surface. The Vickers hardness number (HVN) in GPa was calculated based on the equation shown below:

$$Hv = 1.854 * P / a^2 \quad (3)$$

where, Hv: Vickers Micro Hardness (MPa); P: Indentation Load (N); a: Half The Indentation Diagonal (mm); 1.854: The Geometrical Constant Of The Diamond Pyramid.

## 2.8 X-Ray diffraction analysis

An XRD instrument (Panalytical Company, The Netherlands) was employed to verify the crystalline structures (crystal phase and crystalline size) of the prepared samples. The system was equipped with copper- $\alpha$  radiation at a wavelength ( $\lambda$ ) of 1.5405980 angstrom (Å) which is equal to 0.15405980 (nm), produced at 40kV and 7.5mA emission current. This analysis made it possible to collect the information required to determine the crystal structure and phase information of the prepared samples Pure-3Y-TZP, 3Y-TZP-ZnONPs and 3Y-TZP-SiO<sub>2</sub>NPs after the sintering procedure.

## 2.9 Field-emission scanning electron microscopy analysis

FE-SEM was utilized to determine the nanoparticle's size, shape, and surface morphology. SEM (INSPECT f 50-FEI, Field Electron and Ion Company, The Netherlands) was used to investigate the structure of the sintered, gold-coated samples Pure-3Y-TZP, 3Y-TZP-ZnONPs and 3Y-TZP-SiO<sub>2</sub>NPs.

## 2.10 Antibacterial activity

The potential for antibacterial activity of the manufactured samples, pure-3Y-TZP, 3Y-TZP-ZnONPs, and 3Y-TZP-SiO<sub>2</sub>NPs, was investigated against Gram-positive *Streptococcus mutans* and Gram-negative *Escherichia coli* bacterial strains utilizing an agar well-diffusion assay [48]. Prior to the culturing procedure, about 20 ml of Muller-Hinton (MH) agar medium was aseptically poured into sterile Petri dishes. The bacterial species were gathered from their stock cultures utilizing a sterile wire loop [49]. Following cultivation of the organisms, wells with a diameter of 6mm were drilled into the agar plates using a sterile tip. Into the bored wells, various concentrations of the samples (3Y-TZP, 3Y-TZP-ZnONPs, and 3Y-TZP-SiO<sub>2</sub>NPs) were used. Each (0.001g) of the synthesized samples was weighed just before they were utilized for the antibacterial activity study. 10mL of de-ionized water was used as a dissolving factor. The wells were loaded with 100 $\mu$ L of synthesized samples using a micro-pipette tool. The cultured plates comprising the samples (3Y-TZP, 3Y-TZP-SiO<sub>2</sub>NPs (1.5 wt%), 3Y-TZP-SiO<sub>2</sub>NPs (2 wt%), 3Y-TZP-ZnO NPs (1.5 wt%), 3Y-TZP-ZnO NPs (2 wt%)) and the test organisms were incubated overnight at 37°C before recording and measuring the average diameter of the inhibition zones [50].

## 2.11 Anti-biofilm activity

The biofilm inhibitory effects of 3Y-TZP, 3Y-TZP-ZnONPs, and 3Y-TZP-SiO<sub>2</sub>NPs were determined using the microtiter plate (MtP) assay method [51]. Briefly, bacterial strains were grown in 96-well plates at concentration  $1 \times 10^6$  and then treated with 1mL of 3Y-TZP, 3Y-TZP-ZnONPs, and 3Y-TZP-SiO<sub>2</sub>NPs (at 3.1, 6.25, 12.5, 25, 50, and 100  $\mu$ g/ml concentrations) for 24 hrs. Following the stage of incubation, the medium was removed and the samples were washed with phosphate-buffered saline (pH 7.2). Set aside to air-dry; thereafter, the adhered *S. Mutans* and *E. Coli* were stained with crystal violet dye at a concentration of 0.1%. The excess dye was rinsed two times with distilled water and thoroughly dried. To quantify biofilm growth, 0.2ml of ethanol (95%) was added to the CV-stained wells and incubated with shaking for 2 hrs. Their optical density was determined at 595nm.

## 2.12 Statistical analysis

The data were analyzed statically using the Prisma program

Graph Pad. Data are presented as the mean standard deviation of three experiments. Indicate a statistically significant difference at  $p < 0.05$  [52].

### 3. RESULTS AND DISCUSSION

#### 3.1 Characterization of zinc oxide nanoparticles

The phase purity and crystal structure of the prepared pure ZnO were characterized using X-ray diffraction. Figure 4 shows the XRD patterns obtained from a ZnO NPs powder created by a liquid phase process. The intensity measurements were calculated in the range of  $10.0000 <-> 80.0000$  deg and Step Size:  $0.0400$  deg. using a (voltage:  $40.0$  kV Current:  $30.0$  mA) XRD diffract meter supplied with a Cu ( $1.54060 \text{ \AA}$ ) source. The produced NPs diffraction peaks at angles of  $2\theta = (31.76^\circ, 34.42^\circ, 36.25^\circ, 47.53^\circ, 56.58^\circ, 62.84^\circ, \text{ and } 67.94^\circ)$  are reflections from the cubic lattices of the (100), (002), (101), (102), (110), (103), and (112) crystal planes, respectively. According to the peaks in the X-ray diffraction spectrum of the zinc oxide nanostructure shown in Figure 4, which correspond to JCPDS No. 00-036-14511, zinc oxide nano powder has a hexagonal wurtzite structure.

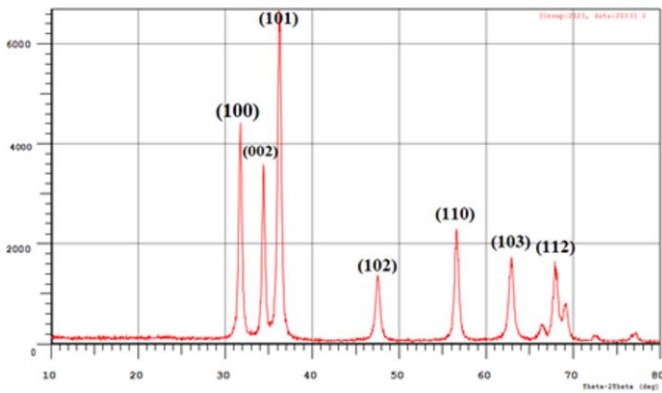


Figure 4. X-ray diffraction of zinc oxide nanoparticles

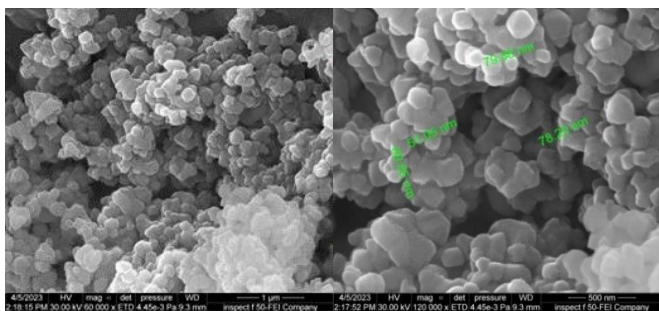


Figure 5. SEM images of zinc oxide nanoparticles

In FE-SEM, the grain size is measured by the distances between the visible grain boundaries. Field Emission Scanning Electron Microscope (FE-SEM) of zinc oxide NPs prepared by a liquid phase process was displayed in Figure 5 provides topographical and elemental information. The FE-SEM analysis image was captured at different magnifications:  $60\ 0000\times$  ,  $120\ 000\times$  . The majority of the ZnO NPs depicted in Figure 4 have a smooth surface, a spherical shape, and exhibiting particle aggregation and agglomeration. The sizes associated with the structures ranged from  $51.05$  nm to  $89.85$  nm. Other studies [53] also observed results that were

comparable.

#### 3.2 Physical properties of prepared nano composite specimens

The density of the (3Y-TZP) matrix is impacted by the presence of zinc oxide NPs, resulting in higher densification and increasing bulk density. The bulk density percentage was shown to increase as the ZnO NPs concentration increased in specimens (D1, E1, and F1) and reached a maximum value in specimen (E1) due to increasing the densification process, resulting in an increase in density. The increase in density clearly indicates the inclusion of zinc oxide nanoparticles into the micro-grain size of  $ZrO_2$ . Hence, the pores on the surface of the grains disappeared rather than increasing in size. Thus, reduced porosity and enhanced densification were the results of this phenomenon [54]. The densification process is regarded as the primary cause of increased mechanical characteristics. When the nanoparticle size is added, the bulk density increases due to the change in the structure of the specimens [55]. In Table 3 provides information on the bulk density, porosity of composite specimen's pure (3Y-TZP) and (3Y-TZP-ZnONPs) sintered at  $1400^\circ\text{C}$  with varying weight percentages of zinc oxide nanoparticles. Figure 6 shows that adding  $1.5$  wt.%,  $2$  wt.%, and  $2.5$  wt.% ZnO NPs to the (3Y-TZP) matrix exerts an effect on the density.

Table 3. Measurement of the bulk density, apparent porosity

No.	Specimen Code	Percentage of SiO <sub>2</sub> Nano Fillers (%)	Bulk Density (g/cm <sup>3</sup> )	Apparent Porosity %
1	A	0	5.05	4.395
2	B2	0.5	4.773	4.35
3	C2	1	5.162	1.183
4	D2	1.5	5.043	0.787
5	E2	2	5.2	1.344
6	F2	2.5	4.832	1.86

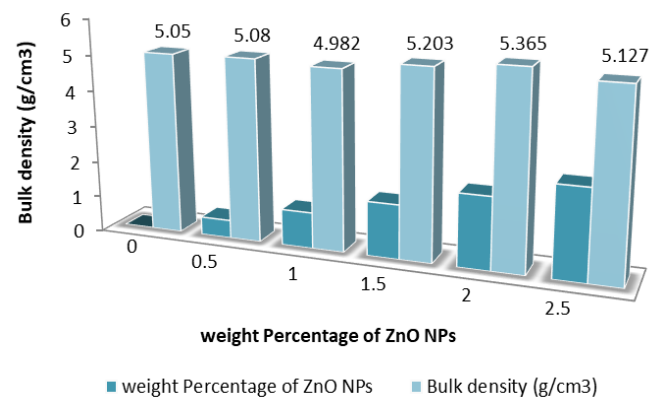
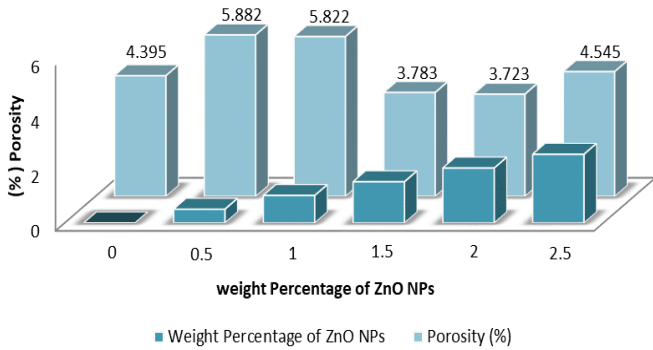


Figure 6. Results of bulk density values in response to adding different weight percentages of ZnO NPs

As shown in Figure 7, The increase in apparent porosity in specimens (B1 and C1) can be attributed to the composite having a weak particle size distribution and poor filling of voids between micro-grains of  $ZrO_2$  and ZnO nanoparticles due to the relatively small amount of zinc oxide NPs that were introduced to the 3Y-TZP matrix.

Furthermore, as the content of zinc oxide nanoparticles increased, the porosity percentage decreased in specimens (D1 and E1) and reached minimum value in a specimen (E1) due

to denser structure development and better particle size distribution in the composite, which were achieved by adding more zinc oxide NPs, which also reduced the porosity. due to the filling of voids between micro grains of the (3Y-TZP) system. The FE-SEM pictures in Figure 8 for specimens (A) and (D1) show that the (3Y-TZP-ZnO NPs) composite was completely densified at 1400°C due to the complete densification of the composite during sintering.



**Figure 7.** Results of apparent porosity values in response to adding different weight percentages of ZnO NPs

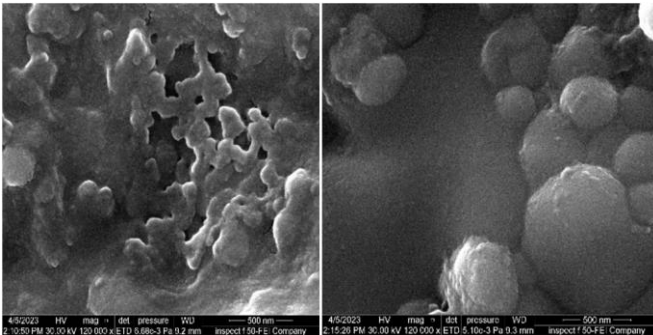


**Figure 8.** FE-SEM images (left panel; scale bar 500nm) for (Pure-3Y-TZP) without adding ZnO NPs and (right panel; scale bar 500nm) for (3Y-TZP-ZnO NPs) with 1.5wt.% ZnO NPs

The case of (3Y-TZP-SiO<sub>2</sub>NPs) as new nano composite was submitted in Table 4 as bulk density, porosity data for Pure-3Y-TZP, and 3Y-TZP-SiO<sub>2</sub>NPs composite specimens sintered at 1400°C with various weight percentages of amorphous precipitated silica nanoparticles. The relation between bulk density and the used weight percentages of SiO<sub>2</sub> NPs are demonstrated in Figure 9. We found that the addition of 1wt%, 1.5wt%, and 2wt% nano-silica to the 3Y-TZP exerts an effect on the density, where the bulk density percentage was shown to increase as the SiO<sub>2</sub>NPs concentration increased in specimens (C2, D2, and E2), which reached a maximum value in specimen (E2) due to increasing the densification process, a result that was also reported by vast previous studies. The key factor increasing the mechanical properties has been determined to be the densification process. When nanoparticles are added, the specimen's changed structural properties cause an increase in bulk density [56].

As shown in Figure 10, the apparent porosity was reduced as the percentage of nano silica additions increased for all specimens after sintering. This is due to denser structure development and reduced porosity of composite specimens, which was decreased to a minimum value in the specimen (D2) (0.787%).

**Table 4.** Measurement of the bulk density, apparent porosity

No.	Code	ZnO Nano Fillers (%)	Bulk Density (g/cm <sup>3</sup> )	Apparent Porosity %
1	A	0	5.05	4.395
2	B1	0.5	5.08	5.882
3	C1	1	4.982	5.822
4	D1	1.5	5.203	3.783
5	E1	2	5.365	3.723
6	F1	2.5	5.127	4.545

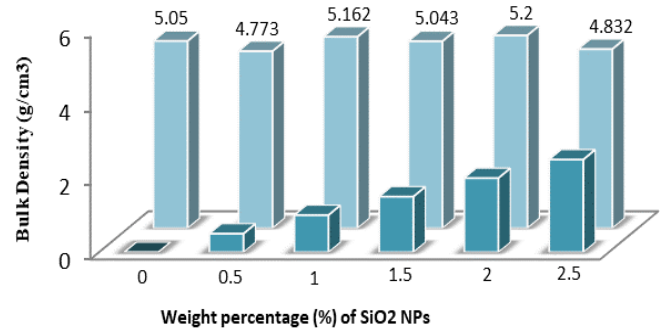


**Figure 9.** Results of bulk density values in response to adding different weight percentages of SiO<sub>2</sub>NPs

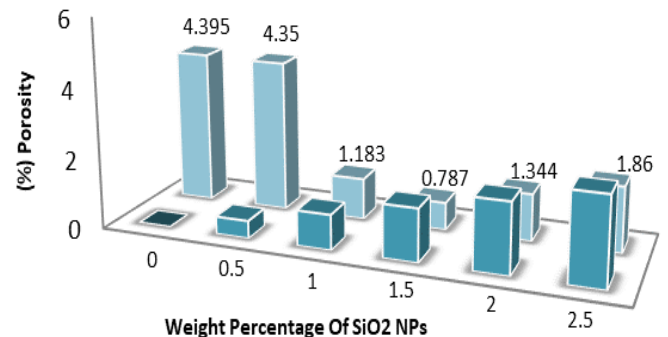


**Figure 10.** Results of apparent porosity values in response to adding different weight percentages of SiO<sub>2</sub>NPs

Moreover, the addition of higher amounts of nano-silica has caused the particles to be better distributed in size. It has also led to a reduction in porosity as a function of the intra-micro grain voids belonging to the voids between 3Y-TZP systems being filled upon adding SiO<sub>2</sub> at the nano-scale level. As sintering progresses, the porosity was decreased as density increased, due to particle convergence, which allows for full particle coalescence and causes the formation of the viscous flow required for densification [57].

Point in specimens (D1, E1, and F1) and reached a maximum value in the specimen (E1) due to increasing the densification process. These high hardness levels were also significantly impacted by a combination of increased density and decreased porosity. The addition of zinc oxide nanoparticles promotes the development of crystal phases, which results in a rise in the Vickers hardness of the manufactured Nano composites.

### 3.3 Mechanical properties of prepared nano composite Specimens hardness by Vickers indentation

A solid material's hardness can be interpreted as its

resistance to being penetrated by another harder material without damaging its surface. Table 5 shows the microhardness results for the samples sintered at 1400°C for 2 hrs with various weight percentages of ZnO NPs. From Figure 11, it can be indicated that the hardness of the nanocomposites is enhanced with the increasing amount of ZnO NPs. There is a significant difference in the hardness value when zinc oxide NPs are added. As a result of the addition of zinc oxide NPs, Moreover, the effect of zinc oxide NPs on inhibiting and reducing cracks developing at the borders of the Vickers indentation is responsible for the increase in hardness. As a result of the addition of zinc oxide NPs, the hardness of the composites produced is more accurate, implying greater durability. The small amounts of zinc oxide nanoparticles e.g., 1.5 wt% and 2 wt% may disperse i.e., permeate and generally diffuse faster in the matrix yttria-stabilized tetragonal zirconia polycrystalline during the sintering process at 1400°C than the larger amounts of zinc oxide nanoparticles for example, 2.5 wt%. As we can see in specimen (F1) if we consider only the chemical interaction effect of ZnO nanoparticles, then a higher amount of ZnO nanoparticles would result in the opposite direction, i.e., a more glassy phase during the sintering process [58]. These results showed that ZnO NPs could increase the composites' hardness. The composites' densification increased dramatically when the ZnO NPs content rose from 0 to 2.5 weight percent. Most likely, the presence of zinc oxide, which was involved in the development of the liquid phase and encouraged high densification, was the cause of the rise in densification [59].

**Table 5.** Measurement of Hardness by Vickers Indentation

Sample Code	Sample Description	Hardness (MPa)
A	3Y-TZP	1279.6
B1	3Y-TZP-0.5wt.%ZnO NPs	1340
C1	3Y-TZP-1wt.%ZnO NPs	1271.5
D1	3Y-TZP-1.5wt.%ZnO NPs	1449
E1	3Y-TZP-2wt.%ZnO NPs	1483.6
F1	3Y-TZP-2.5wt.%ZnO NPs	1395.3
B2	3Y-TZP - 0.5wt.%SiO <sub>2</sub> NPs	1550.6
C2	3Y-TZP-1wt.%SiO <sub>2</sub> NPs	1367.3
D2	3Y-TZP-1.5wt.%SiO <sub>2</sub> NPs	1511.6
E2	3Y-TZP-2wt.%SiO <sub>2</sub> NPs	1381
F2	3Y-TZP-2.5wt.%SiO <sub>2</sub> NPs	1686.6

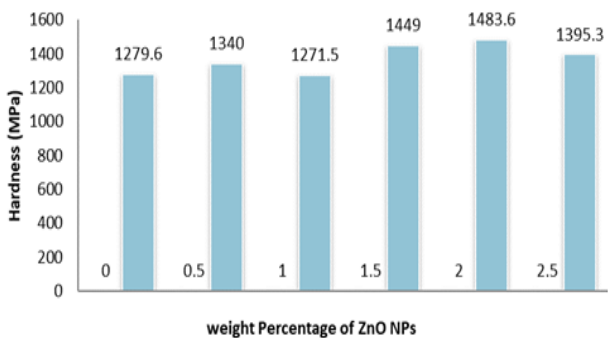


**Figure 11.** The effects of adding ZnO NPs in different weight rates on Vickers microhardness

In the case of (3Y-TZP-SiO<sub>2</sub>NPs), Micro hardness data are represented in Table 5 and Figure 12. A noticeable rise in hardness was seen along with rising the weight of silica NPs. In zirconia-based composites, the incorporation of nano-size-reinforced particles is principally responsible for the increase in average hardness. It is particularly important to note that

both zirconium dioxide and silica nanoparticles are made from ceramic materials, which helps to avoid positional load limitations and deformations of the matrix throughout the hardness test. Also, the matrix and the reinforcement nanoparticles differ in their thermal expansion coefficient values, resulting in a more dense matrix, which causes it to harden [60, 61]. The hardness was at its highest point in specimens (B2, D2, F2) because, as soaking time increases, defects that degrade their mechanical properties are reduced during sintering, leading to full densification.

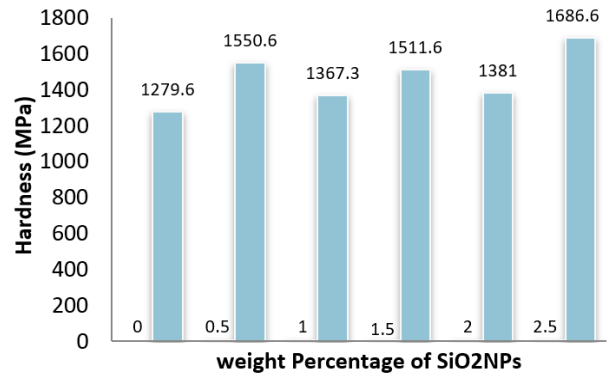


**Figure 12.** The effects of adding SiO<sub>2</sub> NPs in different weight rates on Vickers microhardness

In addition, increased density and decreased porosity exert a substantial impact on these high hardness levels. Nevertheless, toughness does not necessarily improve in more hard surfaces, as it also profoundly impacted by factors like grain size and distribution, as also demonstrated in the present work. Also, an increase in residual surface stresses produced by the interaction of silica nanoparticles with the ceramic matrix substrate (3Y-TZP) might lead to higher hardness, because the reinforcement phase and ceramic substrate have different coefficients of thermal expansion [60]. Eventually, the silica NPs function as a barrier against opposing forces, limiting and restricting other particles' mobility as they pass through one another, as well as their orientation, which leads to a rise in hardness value. Overall, harder surfaces are indicators of higher resistance to the influences of wear and scratch.

As presented in Figure 13, the surfaces morphology, which is generated due to the addition of nanomaterial. The surface morphology of the pure 3Y-TZP, as shown in Figure 13, was analyzed after undergoing 2 hrs of heat treatment at 1400°C.

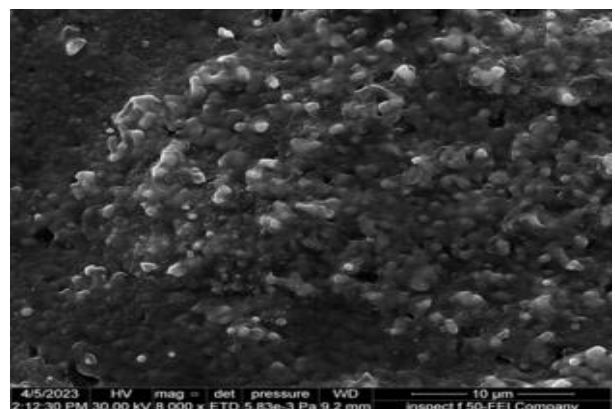


**Figure 13.** The FESEM analysis for the pure 3Y-TZP in different measuring scale

Besides, the addition of the 1.5wt% of (ZnO NPs) to the 3Y-TZP presented different surface morphology, such as spherulical nano particles, as shown in Figure 14.

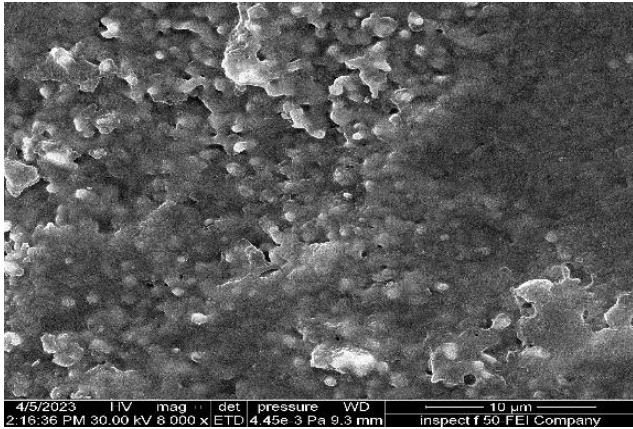


**Figure 14.** The surface morphology of the 3Y-TZP-ZnONP (1.5wt% of (ZnO NPs)

Finally, the surface morphology of the prepared nano composite (3Y-TZP-SiO<sub>2</sub>NPs) specimen, 1.5wt% of (SiO<sub>2</sub>NPs) was presented in Figure 15 and the difference was very clear.

Figure 15 demonstrate that the (3Y-TZP-SiO<sub>2</sub>NPs) composite was entirely densities at 1400°C as a result of complete densification of the composite during sintering.

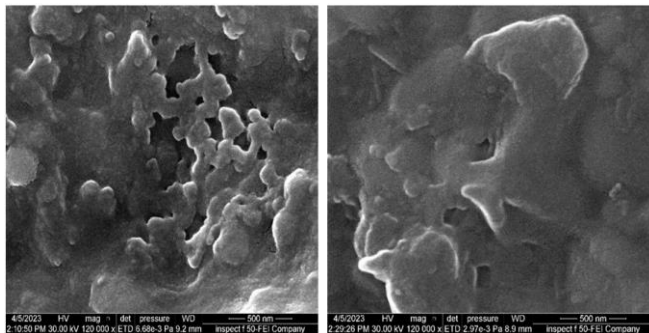


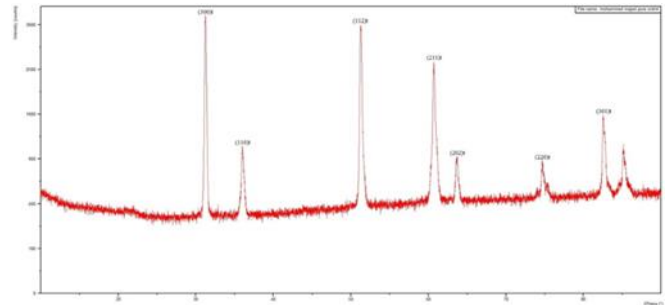
**Figure 15.** The surface morphology of the for the prepared (3Y-TZP-SiO<sub>2</sub>NPs) nanocomposites specimen, 1.5wt% of (SiO<sub>2</sub>NPs)

The reduction in particle size affects a materials mechanical characteristics. It is well understood that lowering the size of grains to the nano scale or forming a nano composite improves the strength of ceramic materials. As a result, when a finer grain size of ZnO is introduced, the hardness of the compacted nano powder composite increases. Because of the reduction in flaws that impair their mechanical characteristics during sintering and the manifestation of full densification, as well as the distribution and size of the grain sizes for the matrix and reinforcement phases.

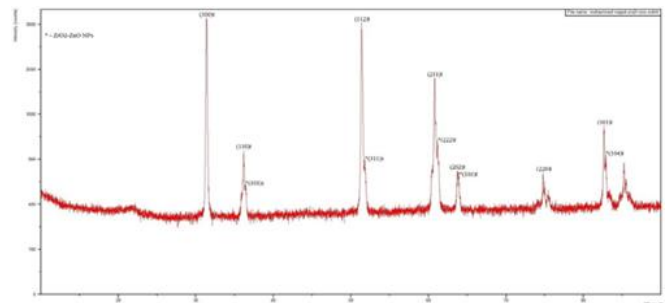
### 3.4 Structural characterization of prepared nano composite specimens, XRD analysis for pure-3Y-TZP, 3Y-TZP-ZnO NPs

Figure 16 shows that the main and only phase formed is tetragonal zirconia (t-ZrO<sub>2</sub>). The structural characterization of pure (3YTZP) after sintering at 1400°C indicates the XRD patterns of the tetragonal ZrO<sub>2</sub> crystal phase as compared to

JCPDS File No. 79-1771 and ICDD 042-1164. Hence, seven significant peaks of t-ZrO<sub>2</sub> were observed. Figure 16 shows the XRD pattern of zirconia, indicating the peaks at 2 $\theta$ =31.25°, 36.01°, 51.17°, 60.57°, 63.58°, 74.66°, 82.78° that correspond to (300), (110), (112), (211), (202), (220), and (301) planes, respectively, indicating that the tetragonal phase is prevalent. In the case of (3Y-TZP-ZnONPs), as shown in Figure 17, the XRD pattern at an angle 2 $\theta$ , exerts twelve peaks at 2 $\theta$ (31.36°, 36.14°, 36.17°, 51.36°, 51.78°, 60.39°, 60.78°, 63.70°, 63.88°, 74.79°, 82.63°, 82.89°), that correspond to (300), (110), (101), (112), (311), (211), (222), (202), (103), (220), (301), and (104) planes.



**Figure 16.** The X-ray diffraction pattern for prepared (Pure 3Y-TZP) nano composite specimen



**Figure 17.** XRD for (3Y-TZP-ZnO NPs) nano composite specimen 1.5 wt% of (ZnO NPs)

Moreover, it was demonstrated that the absence of the monoclinic phase and the vast majority of the peaks matched the (t-ZrO<sub>2</sub>) phase. This was anticipated given that the nano powders employed had been stabilized in the tetragonal phase with the 3mol. yttrium oxide. Furthermore, five new peaks appear after the inclusion of zinc oxide NPs in the matrix of ZrO<sub>2</sub> stabilized with yttrium oxide. The reveals of these five peaks were detected in Figure 17, at 2 $\theta$ =36.17°, 51.78°, 60.78°, 63.88°, 82.89°. Corresponded to planes (101), (311), (222), (103) and (104), respectively. Also, according to Figure 18, the inclusion of ZnO NPs significantly affected the stabilization of zirconia polymorphs, where zinc oxide nanoparticles play a crucial role in inhibiting the monoclinic structure of ZrO<sub>2</sub> and stabilizing the tetragonal phase of ZrO<sub>2</sub>. Moreover, all the tetragonal zirconia (t-ZrO<sub>2</sub>) that contained zinc oxide nanoparticles exhibited strong and sharp peaks. and agreed with the characteristic peaks of hexagonal (wurtzite) crystalline structure as compared to the JCPDS, File No. 00-036-14511.

### 3.5 XRD analysis for pure-3Y-TZP, 3Y-TZP-SiO<sub>2</sub>NPs

As we mentioned before, the structural analysis of pure (3YTZP), as seen in Figure 16, after sintering at (1400°C),

reveals that tetragonal zirconia ( $t\text{-ZrO}_2$ ) is the only phase that forms. (JCPDS 79-1771) and (ICDD 042-1164) were used respectively to identify tetragonal zirconia ( $t\text{-ZrO}_2$ ), and seven significant peaks of  $t\text{-ZrO}_2$  were seen. The XRD pattern of (3YTZP) is shown in Figure 16, with the peaks at  $2\theta = (31.25^\circ, 36.01^\circ, 51.17^\circ, 60.57^\circ, 63.58^\circ, 74.66^\circ, 82.78^\circ)$ , corresponding to (300), (110), (112), (211), (202), (220), and (301) planes, which indicate that the tetragonal phase is predominant.

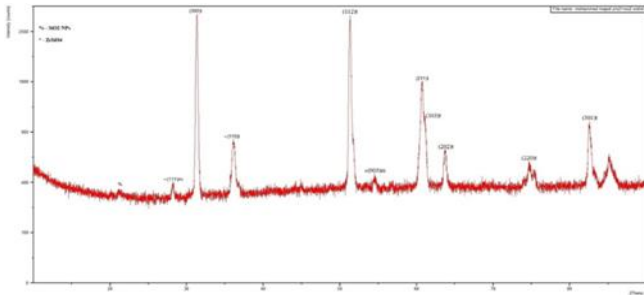


**Figure 18.** X-ray diffraction pattern for the prepared (3Y-TZP -  $\text{SiO}_2\text{NPs}$ ) 1.5wt% of ( $\text{SiO}_2\text{NPs}$ )

In the case of (3Y-TZP- $\text{SiO}_2\text{NPs}$ ), Figure 18 shows the XRD pattern at an angle  $2\theta$ , exerting ten peaks at  $28.20^\circ, 31.32^\circ, 36.02^\circ, 51.34^\circ, 54.49^\circ, 60.61^\circ, 60.80^\circ, 63.74^\circ, 74.75^\circ, 82.48^\circ$ , corresponding to the (111), (300), (110), (112), (003), (103), (211), (202), (220), and (301) planes, respectively. As a result, the main phase formed is tetragonal zirconia ( $t\text{-ZrO}_2$ ). On the other hand, Figure 18 shows the three new peaks that appeared after adding silica nanoparticles, located at angles ( $28.20^\circ$ ), ( $54.49^\circ$ ), ( $60.61^\circ$ ) and corresponding to (111), (003), and (103) planes. The high peak centered at ( $60.61^\circ$ ) (103) is characteristic of the tetragonal crystalline phase, according to the tetragonal zirconia PDF Card No. 00-002-0733, whereas those small peaks at ( $28.20^\circ$ ) (111) and ( $54.49^\circ$ ) (003) are characteristic of the monoclinic phase, according to the JCPDS 37-1484 card. The results presented here point to a mixture of majority tetragonal and minority monoclinic crystal phases, which is typical of zirconia materials after similar-temperature sintering. This was expected given that the powders employed had been stabilized in the tetragonal phase with 3% yttrium oxide. Furthermore, it can be noticed the presence of silica nanoparticles at  $2\theta = 22^\circ$ , according to the PDF Card No. (00-001-0424).

Besides, the two tiny peaks at ( $28.20^\circ$ ) (111) and ( $54.49^\circ$ ) (003) are indicative of the monoclinic phase, and the peak ( $36.02^\circ$ ) (110) of the tetragonal crystalline phase is associated with the development of (Zirconium silicate)  $\text{ZrSiO}_4$  according to the PDF Card No. 00-001-0679. As can be seen in Figure 18.

### 3.6 FE-SEM analysis for pure-3Y-TZP, 3Y-TZP-ZnO NPs

Several FE-SEM images of pure  $\text{ZrO}_2\text{-Y}_2\text{O}_3$  and  $\text{ZrO}_2\text{-Y}_2\text{O}_3\text{-ZnONPs}$  were compared to assess the influence of zinc oxide nanoparticle concentration on specimen surface morphology. The FE-SEM was utilized to evaluate the homogeneity, size, and surface morphology of nanoparticles. The method allows for the acquisition of information about the NPs' size and shape. Data for the (pure-3Y-TZP) and (3Y-TZP-ZnO NPs) composite specimens sintered at  $1400^\circ\text{C}$  for two hrs are shown in Figure 19. According to FE-SEM analysis of  $\text{ZrO}_2\text{-Y}_2\text{O}_3\text{-ZnONPs}$ , the inclusion of zinc oxide considerably changed the grain size of the composite. The

sintering temperature has a significant effect on particle size. The higher temperature enhanced the nano scale and provided more effective zinc nanoparticles before the sintering process.

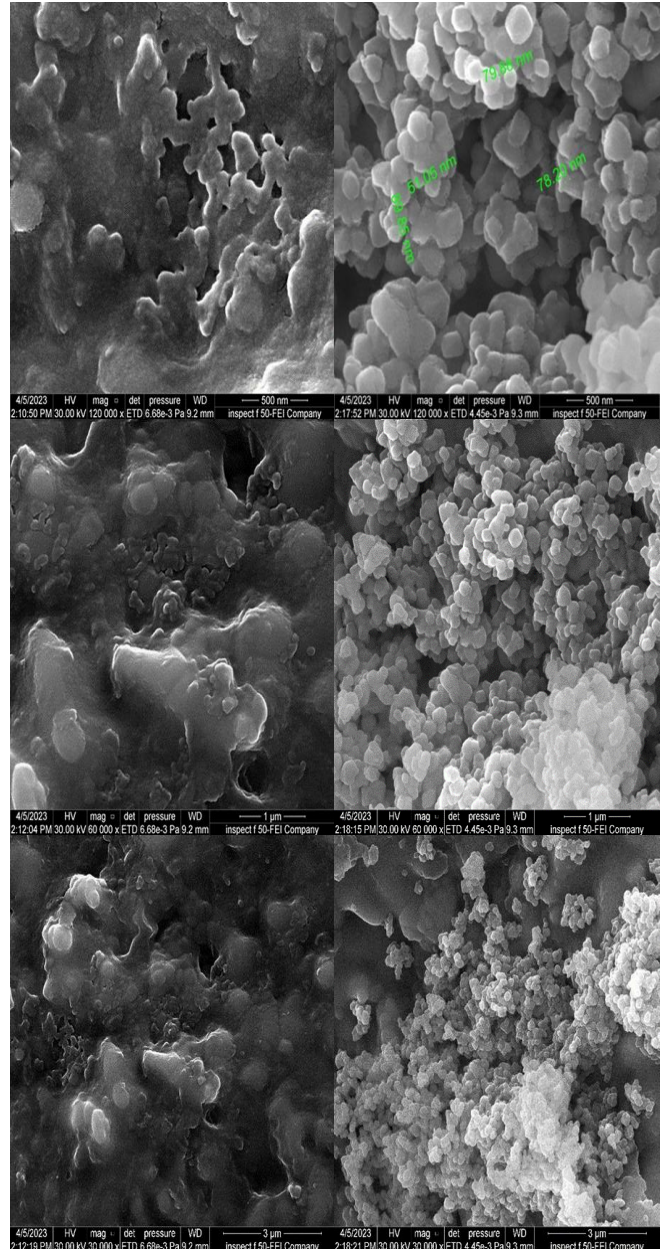


**Figure 19.** FE-SEM pictures (left panels; scale bars 500nm, 1µm, and 3µm) for pure 3Y-TZP along with particle size determinations (right panels; scale bars 500nm, 1µm, and 3µm) for 3Y-TZP-ZnONPs

This could be attributed to all the ceramic oxides employed in the composite being refractory ceramic materials (inorganic compounds), where  $\text{ZrO}_2\text{-Y}_2\text{O}_3$  plays an important role and a quick-acting factor in reducing and inhibiting the grain size of ZnO nanoparticles. Not to mention, zinc oxide is a refractory metal oxide with an extremely high melting point temperature of  $1975^\circ\text{C}$  [62]. Moreover, the higher temperature promoted the nano size and supplied more effective Zn atoms. On the other hand, the oxygen atoms of the zinc oxide compound that are located on the crystal lattice are in an unstable vibrational motion; these oxygen atoms are easier to desorb at higher temperatures, whereas Zr atoms are easier to capture the active oxygen atoms during the sintering process. In summary, there is a random rearrangement of particles in vibrating

superposition as a result of extremely high temperatures. The majority of the ZnO NPs are depicted in Figure 19 as having a smooth surface, a spherical shape, and exhibiting particle aggregation and agglomeration.

### 3.7 FE-SEM analysis for pure-3Y-TZP, 3Y-TZP-SiO<sub>2</sub>NPs

To investigate the influence of silica concentration on specimen surface morphologies, we contrasted FE-SEM images of both the pure ZrO<sub>2</sub>-Y<sub>2</sub>O<sub>3</sub> and chemically modified ZrO<sub>2</sub>-Y<sub>2</sub>O<sub>3</sub>-SiO<sub>2</sub>NPs are presented. The FE-SEM was utilized to assess the size, surface shape, and uniformity of NPs. This technique enabled us to have information about the NPs morphology and size. Figure 20 shows data for (Pure-3Y-TZP) and (3Y-TZP-SiO<sub>2</sub>NPs) composite specimens sintered at 1400°C for 2 hrs.

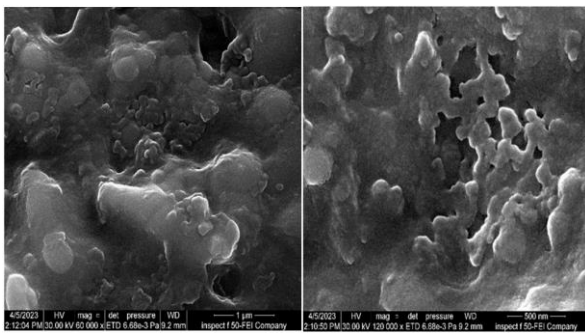


**Figure 20. (a)** The FE-SEM analysis pictures (left panel; scale bar 1 micrometer) along with particle size determination (right panel; scale bar 500 nanometer) for the prepared pure-3Y-TZP nanocomposites specimen

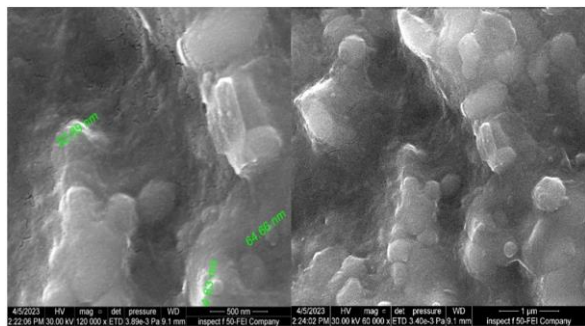


**Figure 20. (b)** The FE-SEM analysis pictures (left panel; scale bar 500 nanometer) along with particle size determinations (right panel; scale bar 1 micrometer) for the prepared 3Y-TZP-SiO<sub>2</sub> NPs nanocomposites specimen, 1.5wt% of (SiO<sub>2</sub> NPs)

According to Figure 20(a) of pure-3Y-TZP, the darker zones indicate porosity near grain boundaries of ZrO<sub>2</sub> grains and the brighter parts represent zirconia stabilized with 3 mole yttrium oxide. On the contrary, as shown in Figure 20(b), 3Y-TZP-SiO<sub>2</sub>NPs, the silica nanoparticles are dispersed uniformly across the ceramic structure and act as a binder material that flows between the zirconia grains to tighten, denser, and reduce the porosity. Furthermore, silica nanoparticles led to the forming of a "glassy phase" within the tetragonal polycrystalline ZrO<sub>2</sub>. The filler produced denser nanoparticles that dispersed properly among the ZrO<sub>2</sub> matrix. Eventually, silica nanoparticles reduce free volume and strengthen the connection within the matrix. In this situation, the mechanical

qualities were improved. To sum it up, Figure 20(b) demonstrates that the 3Y-TZP-SiO<sub>2</sub>NPs was entirely densified at 1400°C as a result of the complete densification of the composite during sintering.

### 3.8 Antibacterial activity

The antibacterial activity results of 3Y-TZP, 3Y-TZP-ZnONPs, and 3Y-TZP-SiO<sub>2</sub>NPs against two highly prevalent oral bacteria using agar well diffusion method shown in Table 6 and Figure 21 indicated that the 3Y-TZP-ZnONPs, and 3Y-TZP-SiO<sub>2</sub>NPs showed inhibiting activities against Gram (+) *S. mutans* and Gram (-) *E.coli* bacterial strains. These findings demonstrated the increased effects of 3Y-TZP on all tested bacteria after reinforcement with ZnO NPs and SiO<sub>2</sub>NPs. In addition, 3Y-TZP-ZnONPs, and 3Y-TZP-SiO<sub>2</sub>NPs inhibited both Gram-positive and Gram-negative isolates in the current investigation while 3Y-TZP did not reveal any antibacterial activity towards any of the bacterial strains. The synthesized 3Y-TZP-ZnONPs had the greatest effect on the growth of *S. mutans* bacteria. The findings of evaluating the effect of zinc oxide nanoparticles demonstrated that they have a much stronger inhibitory effect than, silica nanoparticles against *S. mutans*. This may possibly be because *S. mutans* is more resistant to the SiO<sub>2</sub>NPs employed in this work than *E. coli*. Furthermore, the high efficacy of nanoparticles made of zinc oxide (ZnO), as seen in Figure 21, is due to their tiny size and high surface area, and this enables them to interact with the DNA of bacterial cells, which is another possible explanation. Whereas the antibacterial activity against *E.coli* in both synthesized composites 3Y-TZP-ZnONPs and 3Y-TZP-SiO<sub>2</sub>NPs were proved by the increased diameter of the inhibition zones, as shown in Figure 21b. Furthermore, the 3Y-TZP-SiO<sub>2</sub>NPs showed higher antibacterial activity against Gram-negative bacteria than against Gram-positive bacteria. This is due to variations in the molecular composition of the 'cell walls' of these strains of bacteria. The Gram-negative bacteria have a layer of lipopolysaccharides (LPS) on the outside, with a thin (single-layered) of peptidoglycan underneath. Although (LPS) consist of covalently linked lipids and polysaccharides, they lack rigidity and strength. The negative charges of the lipopolysaccharides (LPS) barrier are attracted to the positive charges available on the nanoparticles. In contrast, the cell walls of Gram-positive bacteria consist primarily of a thick peptidoglycan (multilayered) composed of linear polysaccharide chains cross-linked by short peptides into a three-dimensional rigid structure. Due to the stiffness, less elastic and the expanded networking, the cell walls not only have fewer anchoring points for the NPs but also make their penetration more difficult [62]. For instance, the distinctive mechanisms of nanoparticles can be presented as follows:

The first mechanism, the direct interaction and contact of NPs with the bacterial cell wall causes the breakdown of this wall. When zinc nanoparticles attach to the cell outer membrane and release antibacterial ions, particularly dual-charged e.g. Zn<sup>+2</sup> ions, the cell membrane becomes more permeable, which breaks down the cell wall and results in cell death. The mechanism behind the activities of NPs ions in suppressing microorganisms is that the positive charge on the NPs ions is essential to the substance's antibacterial potency because negatively charged microbe cell membranes electrostatically attract positively charged nanoparticles [63, 64].

The second mechanism, the mechanism of action of zinc oxide as an antibacterial agent depends on the generation of hydrogen peroxide [65]. It is hypothesized that after NPs enter the bacterial cell, they deactivate a few enzymes essential for the organism's metabolic activity, producing hydrogen peroxide (H<sub>2</sub>O<sub>2</sub>). This is due to the existence of nanoparticles that affect *S. mutans* and *E. coli*, this leads to the annihilation of cell components that include proteins, lipids, and DNA which inhibit bacterial growth and ultimately encourage the death of the bacteria.

The third mechanism, the generation of reactive oxygen species (ROS) [66], is responsible for the rise in antibacterial activity with increasing dopant concentration.

The effectiveness of antibacterial against the fixed 3Y-TZP steadily increased as the NPs concentration rose. Furthermore, nanoparticles enhance the generation of (ROS), which leads to the destruction of bacterial cells. These raised ROS have a variety of impacts on bacteria, including lipid peroxidation. This lipid peroxidation compromises the integrity of the bacteria membrane. A lot of membrane leakage develops as a result. Additionally, as the concentration of nanoparticles rises, bacterial mortality is caused by the disintegration of the cell wall [67, 68].

**Table 6.** Antibacterial activity of 3Y-TZP, 3Y-TZP-ZnONPs, and 3Y-TZP-SiO<sub>2</sub>NPs

Antibacterial Analysis (Zone of Inhibition)						
Sample	A	B	C	D	E	F
<i>S. mutans</i>	6	6	7	10	12	18
<i>E. coli</i>	6	6	19	22	24	26

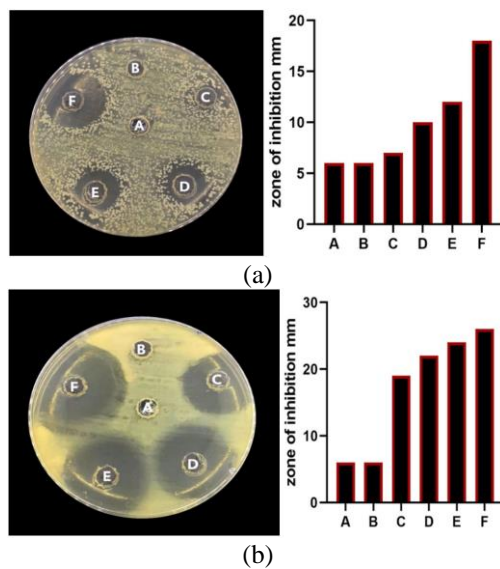


**Figure 21.** Antibacterial activity of (Tested materials) against (a) *S. mutans*.; (b) *E. coli*.

Note: A, control; B, 3Y-TZP; C, 3Y-TZP-SiO<sub>2</sub>NPs (1.5wt%); D, 3Y-TZP-SiO<sub>2</sub>NPs (2wt%); E, 3Y-TZP-ZnONPs (1.5wt%); F, 3Y-TZP-ZnONPs(2wt%)

### 3.9 Effect of prepared nanocomposites on bacterial biofilm by microtiter plate method

At the beginning of any infection, the formation of biofilms is a crucial stage. The formation of microbial biofilms is considered a central virulence factor in localized chronic infections and a major threat to infections [69]. Tooth extraction may occasionally be required because infections caused by bacteria are a significant cause of dental implant

rejection and require intensive treatment [70]. Moreover, bacterial colonization and biofilm formation happen minutes after the implantation process [71]. Additionally, peri-implantitis is a common condition that is one of the primary reasons for implant loss. Biofilms building up in the tissue surrounding the implant are the cause of peri-implantitis, which results in inflammation of the peri-implant mucosa and the gradual degeneration of surrounding tissue [72].

By monitoring the crystal violet (CV) formula's bindings to adherent cells, the effects of 3Y-TZP, 3Y-TZP-ZnONPs, and 3Y-TZP-SiO<sub>2</sub>NPs on biofilm formations were examined in a lab setting. This directly represented the formulations' efficaciousness in inhibiting biofilm formation. The outcome of the 0.1% crystal violet staining assay revealed that all the tested bacteria were capable of creating biofilm, and the 3Y-TZP-based nanocomposites prevented biofilm formation. When treated with various concentrations of 3Y-TZP, 3Y-TZP-ZnONPs, and 3Y-TZP-SiO<sub>2</sub>NPs, it was obvious that the nanocomposites simply eliminated the biofilm. Based on the findings, the most potent inhibitory impact was achieved for 3Y-TZP-ZnONPs nanocomposites.

The untreated control wells were noticed to contain an extremely dense biofilm, while the treated wells failed to produce a biofilm. Figures 22 and 23 summarize the results for *E. Coli* and *S. Mutans* treated with 3Y-TZP and their various nanocomposites at various concentrations. Within 24 hrs of the incubation period, Figure 22a demonstrate that the *E. Coli* cells attached to the untreated well surfaces and produced biofilm. The creation of these biofilms was reduced in the wells treated with 3Y-TZP, 3Y-TZP-ZnONPs, and 3Y-TZP-SiO<sub>2</sub>NPs at different concentrations. Therefore, the 3Y-TZP and their different nanocomposites limit biofilm formation after the initial surface adhesion and maintain the restricted formation of biofilm. The capacity of 3Y-TZP, 3Y-TZP-ZnONPs, and 3Y-TZP-SiO<sub>2</sub>NPs to eliminate the biofilm developed over 24 hrs by the *S. Mutans* strain was also evaluated via a visual contrast between the wells treated with 3Y-TZP, 3Y-TZP-ZnONPs, and 3Y-TZP-SiO<sub>2</sub>NPs and those of the negative control (untreated wells). A noticeable drop in the color intensity of crystal violet was detected in wells treated with 3Y-TZP and their different nanocomposites at different concentrations, exhibiting good anti-biofilm efficacy towards the biofilm produced by the *S. Mutans* strain (Figure 23a).

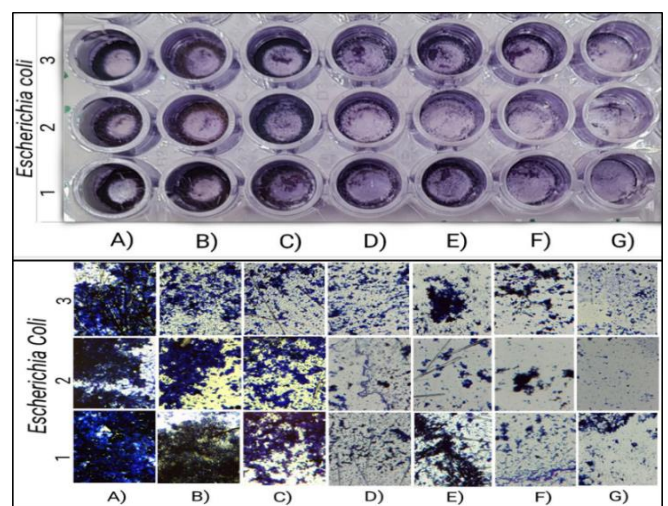


**Figure 22a.** Biofilm formation in *Escherichia Coli* (1, ZrO<sub>2</sub> Pure. 2, ZrO<sub>2</sub>+ ZnO NPs (2). 3, ZrO<sub>2</sub>+SiO<sub>2</sub> NPs (2) reduces)

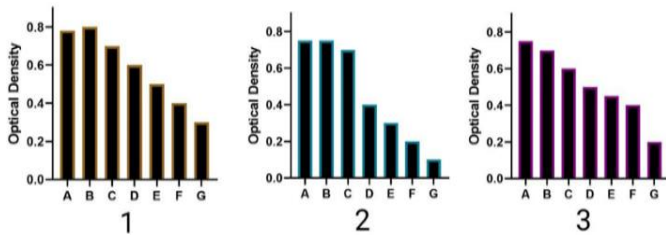


**Figure 22b.** Biofilm formation in *EscherichiaColi* (1, ZrO<sub>2</sub> Pure. 2, ZrO<sub>2</sub>+ ZnO NPs (2). 3, ZrO<sub>2</sub>+SiO<sub>2</sub> NPs (2) reduces.)

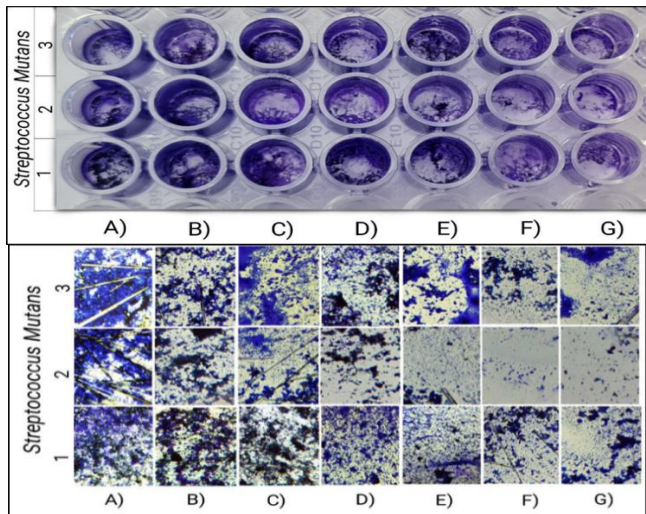


**Figure 23a.** Biofilm formation in *Streptococcus* (1, ZrO<sub>2</sub> Pure. 2, ZrO<sub>2</sub>+ ZnO NPs (2). 3, ZrO<sub>2</sub>+SiO<sub>2</sub> NPs (2) reduces.)

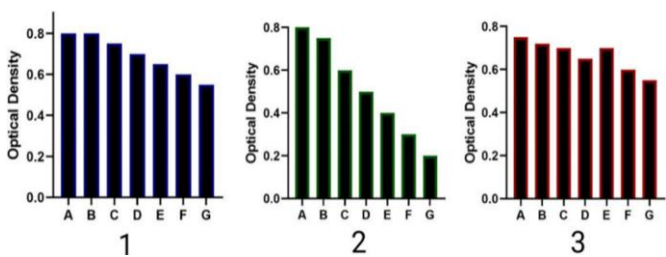


**Figure 23b.** Biofilm formation in *Streptococcus Mutans* (1, ZrO<sub>2</sub> Pure. 2, ZrO<sub>2</sub>+ZnO NPs (2). 3, ZrO<sub>2</sub>+SiO<sub>2</sub> NPs (2) reduces.)

To explain these effects, several theories have been proposed:

- (i) These reductions were likely caused by the generation of ROS, which led to the rupture of the bacterial cells [72].
- (ii) The nanoparticles eliminate the creation of biofilm through their direct interaction with the bacterial cell wall, causing the breakdown of this wall and hindering the growth of biofilms [62, 63].

#### 4. CONCLUSIONS

The following conclusions can be drawn from the study's results:

(1) A mixture of zirconium oxide microcrystals stabilized with the addition of 3 mol. of yttrium oxide and reinforcement with Zinc oxide and Silica Nanoparticles was found to exhibit excellent properties. In addition to the outstanding physical and mechanical properties.

(2) X-ray diffraction analysis of the sintered specimens revealed that the absence of the monoclinic phase and the vast

majority of the peaks matched the (t-ZrO<sub>2</sub>) phase. Also the inclusion of ZnO NPs significantly affected the stabilization of zirconia polymorphs, where zinc oxide nanoparticles play a crucial role in inhibiting the monoclinic structure of ZrO<sub>2</sub> and stabilizing the tetragonal phase of ZrO<sub>2</sub>. Also, XRD results showed a mixture of majority (tetragonal) and minority (monoclinic, with just two tiny, barely noticeable peaks), which is typical of zirconia materials after similar-temperature sintering.

(3) In FE-SEM analysis, the sintering temperature has a significant effect on particle size of ZnO NPs. And the majority of the ZnO NPs are depicted as having a smooth surface, a spherical shape. The silica Nanoparticles are dispersed uniformly across the ceramic structure and act as a binder material that flows between the zirconia grains. Furthermore, silica nanoparticles led to the forming of a "glassy phase" within the tetragonal polycrystalline ZrO<sub>2</sub>. And dispersed properly among the ZrO<sub>2</sub> matrix.

(4) The translucent quality of the prepared composites is a good match for the surrounding tissues within the oral cavity, and has a very high aesthetic appearance. Except for the ones containing 2.5wt% SiO<sub>2</sub> NPs, which indicated a slightly decreased translucency and an increased opacity.

#### ACKNOWLEDGMENT

The researchers would like to thank the Department of Applied Sciences, University of Technology, Iraq.

#### REFERENCES

- [1] Bannunah, A.M. (2023). Biomedical applications of zirconia-based nanomaterials: Challenges and future perspectives. *Molecules*, 28(14): 5428. <http://doi.org/10.3390/molecules28145428>
- [2] Bilensoy, E., Varan, C. (2023). Is there a niche for zinc oxide nanoparticles in future drug discovery?. *Expert Opinion on Drug Discovery*, 18(9): 943-945. <https://doi.org/10.1080/17460441.2023.2230152>
- [3] Raj, S., Jose, S., Sumod, U.S., Sabitha, M. (2012). Nanotechnology in cosmetics: Opportunities and challenges. *Journal of Pharmacy and Bioallied Sciences*, 4(3): 186-193. <https://doi.org/10.4103/0975-7406.99016>
- [4] Marques, A.C., Vale, M., Vicente, D., Schreck, M., Tervoort, E., Niederberger, M. (2021). Porous silica microspheres with immobilized titania nanoparticles for in-flow solar-driven purification of wastewater. *Global Challenges*, 5(5): 2000116. <https://doi.org/10.1002/gch2.202000116>
- [5] Thomas, S., Baiju, R.M. (Eds.). (2023). *Nanomaterials in dental medicine*. Springer Nature. 33-111. <https://doi.org/10.1007/978-981-19-8718-2>
- [6] Shillitoe, E., Weinstock, R., Kim, T., Simon, H., Planer, J., Noonan, S., Cooney, R. (2012). The oral microflora in obesity and type-2 diabetes. *Journal of Oral Microbiology*, 4(1): 19013. <https://doi.org/10.3402/jom.v4i0.19013>
- [7] Gronwald, B., Kozłowska, L., Kijak, K., Lietz-Kijak, D., Skomro, P., Gronwald, K., Gronwald, H. (2023). Nanoparticles in dentistry-current literature review. *Coatings*, 13(1): 102. <https://doi.org/10.3390/coatings1301012>

- [8] Padrós, R., Giner-Tarrida, L., Herrero-Climent, M., Punset, M., Gil, F.J. (2020). Corrosion resistance and ion release of dental prosthesis of CoCr obtained by CAD-CAM milling, casting and laser sintering. *Metals*, 10(6): 827. <https://doi.org/10.3390/met10060827>
- [9] Aksoy, G., Polat, H., Polat, M., Coskun, G. (2006). Effect of various treatment and glazing (coating) techniques on the roughness and wettability of ceramic dental restorative surfaces. *Colloids and Surfaces B: Biointerfaces*, 53(2): 254-259. <https://doi.org/10.1016/j.colsurfb.2006.09.016>
- [10] Tan, K., Pjetursson, B.E., Lang, N.P., Chan, E.S. (2004). A systematic review of the survival and complication rates of fixed partial dentures (FPDs) after an observation period of at least 5 years: III. Conventional FPDs. *Clinical oral Implants Research*, 15(6): 654-666. <https://doi.org/10.1111/j.1600-0501.2004.01119.x>
- [11] Pjetursson, B.E., Sailer, I., Makarov, N.A., Zwahlen, M., Thoma, D.S. (2015). All-ceramic or metal-ceramic tooth-supported fixed dental prostheses (FDPs)? A systematic review of the survival and complication rates. Part II: Multiple-unit FDPs. *Dental Materials*, 31(6): 624-639. <http://doi.org/10.1016/j.dental.2015.02.013>
- [12] Denry, I., Kelly, J.R. (2008). State of the art of zirconia for dental applications. *Dental Materials*, 24(3): 299-307. <http://doi.org/10.1016/j.dental.2007.05.007>
- [13] Miyazaki, T., Nakamura, T., Matsumura, H., Ban, S., Kobayashi, T. (2013). Current status of zirconia restoration. *Journal of Prosthodontic Research*, 57(4): 236-261. <https://doi.org/10.1016/j.jpor.2013.09.001>
- [14] Pittayachawan, P. (2009). Comparative study of physical properties of zirconia based dental ceramics. Doctoral dissertation, UCL (University College London), pp. 27-28. <https://discovery.ucl.ac.uk/id/eprint/14476>
- [15] Wang, Z., Xia, J., Xia, Y., Lu, C., Shi, G., Zhang, F., Zhu, F., Li, Y., Xia, L., Tang, J. (2013). Fabrication and characterization of a zirconia/multi-walled carbon nanotube mesoporous composite. *Materials Science and Engineering: C*, 33(7): 3931-3934. <https://doi.org/10.1016/j.msec.2013.05.031>
- [16] AL-AMLEH, B., Lyons, K., Swain, M. (2010). Clinical trials in zirconia: A systematic review. *Journal of Oral Rehabilitation*, 37(8): 641-652. <https://doi.org/10.1111/j.1365-2842.2010.02094.x>
- [17] Aboushelib, M.N., Feilzer, A.J., Kleverlaan, C.J. (2010). Bonding to zirconia using a new surface treatment. *Journal of Prosthodontics: Implant, Esthetic and Reconstructive Dentistry*, 19(5): 340-346. <http://doi.org/10.1111/j.1532-849X.2010.00575.x>
- [18] Mattiello, R.D.L., Coelho, T.M.K., Insaurralde, E., Coelho, A.A.K., Terra, G.P., Kasuya, A.V.B., Favarão, I.N., de Souza Gonçalves, L., Fonseca, R.B. (2013). A review of surface treatment methods to improve the adhesive cementation of zirconia-based ceramics. *ISRN Biomaterials*, 2013: 1-10. <https://doi.org/10.5402/2013/185376>
- [19] Melo, R.M., Souza, R.O.A., Dursun, E., Monteiro, E.B.C., Valandro, L.F., Bottino, M.A. (2015). Surface treatments of zirconia to enhance bonding durability. *Operative Dentistry*, 40(6): 636-643. <https://doi.org/10.2341/14-144-L>
- [20] Hjerpe, J., Närhi, T., Fröberg, K., Vallittu, P.K., Lassila, L.V. (2008). Effect of shading the zirconia framework on biaxial strength and surface microhardness. *Acta Odontologica Scandinavica*, 66(5): 262-267. <https://doi.org/10.1080/00016350802247123>
- [21] Jin, G., Qin, H., Cao, H., Qian, S., Zhao, Y., Peng, X., Zhang, X., Liu, X., Chu, P.K. (2014). Synergistic effects of dual Zn/Ag ion implantation in osteogenic activity and antibacterial ability of titanium. *Biomaterials*, 35(27): 7699-7713. <https://doi.org/10.1016/j.biomaterials.2014.05.074>
- [22] Wang, R., He, X., Gao, Y., Zhang, X., Yao, X., Tang, B. (2017). Antimicrobial property, cytocompatibility and corrosion resistance of Zn-doped ZrO<sub>2</sub>/TiO<sub>2</sub> coatings on Ti6Al4V implants. *Materials Science and Engineering: C*, 75: 7-15. <https://doi.org/10.1016/j.msec.2017.02.036>
- [23] Kharisov, B.I. (2008). A review for synthesis of nanoflowers. *Recent Patents on Nanotechnology*, 2(3): 190-200. <http://doi.org/10.2174/187221008786369651>
- [24] Özgür, Ü., Alivov, Y.I., Liu, C., Teke, A., Reshchikov, M.A., Doğan, S., Avrutin, V., Cho, S.J., Morkoç, A.H. (2005). A comprehensive review of ZnO materials and devices. *Journal of Applied Physics*, 98(4). <https://doi.org/10.1063/1.1992666>
- [25] Moezzi, A., McDonagh, A.M., Cortie, M.B. (2012). Zinc oxide particles: Synthesis, properties and applications. *Chemical Engineering Journal*, 185: 1-22. <https://doi.org/10.1016/j.cej.2012.01.076>
- [26] Memarzadeh, K., Sharili, A.S., Huang, J., Rawlinson, S.C., Allaker, R.P. (2015). Nanoparticulate zinc oxide as a coating material for orthopedic and dental implants. *Journal of Biomedical Materials Research Part A*, 103(3): 981-989. <https://doi.org/10.1002/jbm.a.35241>
- [27] Khan, A.S., Farooq, I., Alakrawi, K.M., Khalid, H., Saadi, O.W., Hakeem, A.S. (2020). Dentin tubule occlusion potential of novel dentifrices having fluoride containing bioactive glass and zinc oxide nanoparticles. *Medical Principles and Practice*, 29(4): 338-346. <https://doi.org/10.1159/000503706>
- [28] Toledano-Osorio, M., Osorio, E., Aguilera, F.S., Medina-Castillo, A.L., Toledano, M., Osorio, R. (2018). Improved reactive nanoparticles to treat dentin hypersensitivity. *Acta Biomaterialia*, 72: 371-380. <https://doi.org/10.1016/j.actbio.2018.03.033>
- [29] Toledano, M., Cabello, I., Osorio, E., Aguilera, F.S., Medina-Castillo, A.L., Toledano-Osorio, M., Osorio, R. (2019). Zn-containing polymer nanogels promote cervical dentin remineralization. *Clinical Oral Investigations*, 23: 1197-1208. <https://doi.org/10.1007/s00784-018-2548-1>
- [30] Verma, R., Chauhan, A., Shandilya, M., Li, X., Kumar, R., Kulshrestha, S. (2020). Antimicrobial potential of Ag-doped ZnO nanostructure synthesized by the green method using *Moringa oleifera* extract. *Journal of Environmental Chemical Engineering*, 8(3): 103730. <https://doi.org/10.1016/j.jece.2020.103730>
- [31] Carofiglio, M., Barui, S., Cauda, V., Laurenti, M. (2020). Doped zinc oxide nanoparticles: Synthesis, characterization and potential use in nanomedicine. *Applied Sciences*, 10(15): 5194. <http://doi.org/10.3390/app10155194>
- [32] Abebe, B., Zereffa, E.A., Tadesse, A., Murthy, H.A. (2020). A review on enhancing the antibacterial activity of ZnO: Mechanisms and microscopic investigation. *Nanoscale Research Letters*, 15: 1-19. <http://doi.org/10.1186/s11671-020-03418-6>
- [33] Attia, M.S., Yahya, A., Monaem, N.A., Sabry, S.A.

- (2023). Mesoporous silica nanoparticles: Their potential as drug delivery carriers and nanoscavengers in Alzheimer's and Parkinson's diseases. *Saudi Pharmaceutical Journal*, 31(3): 417-432. <https://doi.org/10.1016/j.jsps.2023.01.009>
- [34] Gonçalves, M.C. (2018). Sol-gel silica nanoparticles in medicine: A natural choice. *Design, Synthesis and Products. Molecules*, 23(8): 2021. <http://doi.org/10.3390/molecules23082021>
- [35] Lee, D.W., Yoo, B.R. (2016). Advanced silica/polymer composites: Materials and applications. *Journal of Industrial and Engineering Chemistry*, 38: 1-12. <https://doi.org/10.1016/j.jiec.2016.04.016>
- [36] Khormi, A.Y., Al-Shehri, B.M., Al-Zahrani, F.A., Hamdy, M.S., Fouda, A., Shaaban, M.R. (2023). Palladium nanoparticles incorporated fumed silica as an efficient catalyst for nitroarenes reduction via thermal and microwave heating. *Catalysts*, 13(2): 445. <http://doi.org/10.3390/catal13020445>
- [37] Manzano, M., Vallet-Regí, M. (2020). Mesoporous silica nanoparticles for drug delivery. *Advanced Functional Materials*, 30(2): 1902634. <http://doi.org/10.1002/adfm.2019.02634>
- [38] Croissant, J.G., Butler, K.S., Zink, J.I., Brinker, C.J. (2020). Synthetic amorphous silica nanoparticles: Toxicity, biomedical and environmental implications. *Nature Reviews Materials*, 5(12): 886-909. <https://doi.org/10.1038/s41578-020-0230-0>
- [39] Arts, J.H., Muijser, H., Duistermaat, E., Junker, K., Kuper, C.F. (2007). Five-day inhalation toxicity study of three types of synthetic amorphous silicas in Wistar rats and post-exposure evaluations for up to 3 months. *Food and Chemical Toxicology*, 45(10): 1856-1867. <https://doi.org/10.1016/j.fct.2007.04.001>
- [40] Nekounam, H., Malakootikhah, J., Shaterabadi, D., Negahdari, B., Kandi, M.R., Hamblin, M.R. (2023). Silica NPs-Cytotoxicity Cross-Talk: Physicochemical principles and cell biology responses. *Silicon*, 15(13): 5455-5465. <https://doi.org/10.1007/s12633-023-02407-5>
- [41] Tang, L., Cheng, J. (2013). Nonporous silica nanoparticles for nanomedicine application. *Nano Today*, 8(3): 290-312. <https://doi.org/10.1016/j.nantod.2013.04.007>
- [42] Bitar, A., Ahmad, N.M., Fessi, H., Elaissari, A. (2012). Silica-based nanoparticles for biomedical applications. *Drug Discovery Today*, 17(19-20): 1147-1154. <http://dx.doi.org/10.1016/j.drudis.2012.06.014>
- [43] Bruckmann, F.D.S., Nunes, F.B., Salles, T.D.R., Franco, C., Cadoná, F.C., Bohn Rhoden, C.R. (2022). Biological applications of silica-based nanoparticles. *Magnetochemistry*, 8(10): 131. <https://doi.org/10.3390/magnetochemistry8100131>
- [44] He, Y., Li, J., Long, M., Liang, S., Xu, H. (2017). Tuning pore size of mesoporous silica nanoparticles simply by varying reaction parameters. *Journal of Non-Crystalline Solids*, 457: 9-12. <https://doi.org/10.1016/j.jnoncrysol.2016.11.023>
- [45] Kanugala, S., Jinka, S., Puvvada, N., Banerjee, R., Kumar, C.G. (2019). Phenazine-1-carboxamide functionalized mesoporous silica nanoparticles as antimicrobial coatings on silicone urethral catheters. *Scientific Reports*, 9(1): 6198. <https://doi.org/10.1038/s41598-019-42722-9>
- [46] Sripanyakorn, S., Jugdaohsingh, R., Dissayabutr, W., Anderson, S.H., Thompson, R.P., Powell, J.J. (2009). The comparative absorption of silicon from different foods and food supplements. *British Journal of Nutrition*, 102(6): 825-834. <https://doi.org/10.1017/S0007114509311757>
- [47] Al-Karam, L.Q., Majeed, S.M. (2019). Preparation and study to characterize the zno-pva nano composite and its antibacterial effects. *Biochemical & Cellular Archives*, 19(2): 3641-3646. <http://doi.org/10.35124/bca.2019.19.2.3641>
- [48] Bahjat, H.H., Ismail, R.A., Sulaiman, G.M., Jabir, M.S. (2021). Magnetic field-assisted laser ablation of titanium dioxide nanoparticles in water for anti-bacterial applications. *Journal of Inorganic and Organometallic Polymers and Materials*, 31(9): 3649-3656. <https://doi.org/10.21203/rs.3.rs-176836/v1>
- [49] Khashan, K.S., Badr, B.A., Sulaiman, G.M., Jabir, M.S., Hussain, S.A. (2021). Antibacterial activity of Zinc Oxide nanostructured materials synthesis by laser ablation method. In *Journal of Physics: Conference Series*. IOP Publishing, 1795(1): 012040. <https://doi.org/10.1088/1742-6596/1795/1/012040>
- [50] Jihad, M.A., Noori, F.T., Jabir, M.S., Albukhaty, S., AlMalki, F.A., Alyamani, A.A. (2021). Polyethylene glycol functionalized graphene oxide nanoparticles loaded with nigella sativa extract: A smart antibacterial therapeutic drug delivery system. *Molecules*, 26(11): 3067. <https://doi.org/10.3390/molecules26113067>
- [51] Al Rugaie, O., Jabir, M.S., Mohammed, M.K., Abbas, R.H., Ahmed, D.S., Sulaiman, G.M., Mohammed, S.A.A., Khan, R.A., Al-Regaiey, K.A., Alsharidah, M., Mohany, K.M., Mohammed, H.A. (2022). Modification of SWCNTs with hybrid materials ZnO-Ag and ZnO-Au for enhancing bactericidal activity of phagocytic cells against *Escherichia coli* through NOX2 pathway. *Scientific Reports*, 12(1): 17203. <https://doi.org/10.1038/s41598-022-22193-1>
- [52] Jabir, M.S., Rashid, T.M., Nayef, U.M., Albukhaty, S., AlMalki, F.A., Albaqami, J., AlYamani, A.A., Taqi, Z.J., Sulaiman, G.M. (2022). Inhibition of *Staphylococcus aureus*  $\alpha$ -hemolysin production using nanocurcumin capped Au@ ZnO nanocomposite. *Bioinorganic Chemistry and Applications*, 2022. <https://doi.org/10.1155/2022/2663812>
- [53] Zhang, L., Jiang, Y., Ding, Y., Povey, M., York, D. (2007). Investigation into the antibacterial behaviour of suspensions of ZnO nanoparticles (ZnO nanofluids). *Journal of Nanoparticle Research*, 9: 479-489. <http://doi.org/10.1007/s11051-006-9150-1>
- [54] Zaidan, S.A., Majeed, S.M. (2015). Effect of MgAl2O4 particles on characterization of Y2O3-ZrO2 system. *Engineering and Technology Journal*, 33(4 Part): 621-630. <http://doi.org/10.30684/etj.33.4B.6>
- [55] Saad, S.M., Hadi, E.M., Hussien, N.N. (2022). Zirconia-Yttria system for manufacturing ceramic dental. *International Journal of Nanoelectronics & Materials*, 15: 37-47.
- [56] Shi, L.W., Wang, L.J., Jiang, W., Luo, W. (2016). Preparation of highly transparent silica glass by SPS sintering of SBA-15. In *Materials Science Forum*. Trans Tech Publications Ltd, 848: 312-318. <https://doi.org/10.4028/www.scientific.net/MSF.848.312>
- [57] Jin, H.B., Oktar, F.N., Dorozhkin, S., Agathopoulos, S.

- (2011). Sintering behavior and properties of reinforced hydroxyapatite/TCP biphasic bioceramics with ZnO-whiskers. *Journal of Composite Materials*, 45(13): 1435-1445. <https://doi.org/10.1177/0021998310383728>
- [58] Feng, P., Wei, P., Shuai, C., Peng, S. (2014). Characterization of mechanical and biological properties of 3-D scaffolds reinforced with zinc oxide for bone tissue engineering. *PloS One*, 9(1): e87755. <https://doi.org/10.1371/journal.pone.0087755>
- [59] Acchar, W., Zollfrank, C., Greil, P. (2006). Microstructure of alumina reinforced with tungsten carbide. *Journal of Materials Science*, 41: 3299-3302. <https://doi.org/10.1007/s10853-005-5457-z>
- [60] Nai, S.M.L., Kuma, J.V.M., Alam, M.E., Zhong, X.L., Babaghorbani, P., Gupta, M. (2010). Using microwave-assisted powder metallurgy route and nano-size reinforcements to develop high-strength solder composites. *Journal of Materials Engineering and Performance*, 19: 335-341. <https://doi.org/10.1007/s11665-009-9481-z>
- [61] Salman, Z.A., Hubeatir, K.A., Zaidan, S.A. (2021). Effect of CO<sub>2</sub> laser on glazed zircon surface complemented by ZrO<sub>2</sub> Oxide. *Engineering and Technology Journal*, 39(1B): 252-261. <https://doi.org/10.30684/etj.v39i1B.1552>
- [62] Sharma, N., Jandaik, S., Kumar, S. (2016). Synergistic activity of doped zinc oxide nanoparticles with antibiotics: Ciprofloxacin, ampicillin, fluconazole and amphotericin B against pathogenic microorganisms. *Anais da Academia Brasileira de Ciências*, 88: 1689-1698. <https://doi.org/10.1590/0001-3765201620150713>
- [63] Brayner, R., Ferrari-Iliou, R., Brivois, N., Djediat, S., Benedetti, M.F., Fiévet, F. (2006). Toxicological impact studies based on *Escherichia coli* bacteria in ultrafine ZnO nanoparticles colloidal medium. *Nano Letters*, 6(4): 866-870. <https://doi.org/10.1021/nl052326h>
- [64] Kasemets, K., Ivask, A., Dubourguier, H.C., Kahru, A. (2009). Toxicity of nanoparticles of ZnO, CuO and TiO<sub>2</sub> to yeast *Saccharomyces cerevisiae*. *Toxicology in Vitro*, 23(6): 1116-1122. <https://doi.org/10.1016/j.tiv.2009.05.015>
- [65] Emami-Karvani, Z., Chehrizi, P. (2011). Antibacterial activity of ZnO nanoparticle on gram-positive and gram-negative bacteria. *African Journal of Microbiology Research*, 5(12): 1368-1373. <https://doi.org/10.5897/AJMR10.159>
- [66] Selvarajan, V., Obuobi, S., Ee, P.L.R. (2020). Silica nanoparticles—A versatile tool for the treatment of bacterial infections. *Frontiers in Chemistry*, 8: 602. <https://doi.org/10.3389/fchem.2020.00602>
- [67] Tiwari, V., Mishra, N., Gadani, K., Solanki, P.S., Shah, N.A., Tiwari, M. (2018). Mechanism of anti-bacterial activity of zinc oxide nanoparticle against carbapenem-resistant *Acinetobacter baumannii*. *Frontiers in Microbiology*, 9: 1218. <https://doi.org/10.3389/fmicb.2018.01218>
- [68] Chelliah, P., Wabaidur, S.M., Sharma, H.P., Majdi, H.S., Smail, D.A., Najm, M.A., Iqbal, A., Lai, W.C. (2023). Photocatalytic organic contaminant degradation of green synthesized ZrO<sub>2</sub> NPs and their antibacterial activities. *Separations*, 10(3): 156. <https://doi.org/10.3390/separations10030156>
- [69] Matter, M.T., Maliqi, L., Keevend, K., Guimond, S., Ng, J., Armagan, E., Rottmar, M., Herrmann, I.K. (2021). One-step synthesis of versatile antimicrobial nano-architected implant coatings for hard and soft tissue healing. *ACS Applied Materials & Interfaces*, 13(28): 33300-33310. <https://doi.org/10.1021/acsmi.1c10121>
- [70] Alves, C.H., Russi, K.L., Rocha, N.C., Bastos, F., Darrieux, M., Parisotto, T.M., Girardello, R. (2022). Host-microbiome interactions regarding peri-implantitis and dental implant loss. *Journal of Translational Medicine*, 20(1): 425. <https://doi.org/10.1186/s12967-022-03636-9>
- [71] Berglundh, T., Armitage, G., Araujo, M.G., Avila-Ortiz, G., Blanco, J., Camargo, P.M., Chen, S., Cochran, D., Derks, J., Figuero, C.E., Hämmerle, H.F., Heitz-Mayfield, L.J.A., Huynh-Ba, G., Iacono, V., Koo, K.T., Lambert, F., McCauley, L., Quirynen, M., Renvert, S., Salvi, G.E., Schwarz, F., Tarnow, D., Tomasi, C., Wang, H.L., Zitzmann, N. (2018). Peri-implant diseases and conditions: Consensus report of workgroup 4 of the 2017 world workshop on the classification of periodontal and peri-implant diseases and conditions. *Journal of Periodontology*, 89: S313-S318. <https://doi.org/10.1002/JPER.17-0739>
- [72] Dwivedi, S., Wahab, R., Khan, F., Mishra, Y.K., Musarrat, J., Al-Khedhairy, A.A. (2014). Reactive oxygen species mediated bacterial biofilm inhibition via zinc oxide nanoparticles and their statistical determination. *PloS One*, 9(11): e111289. <https://doi.org/10.1371/journal.pone.0111289>

## NOMENCLATURE

NPs	Nanoparticles
3Y	TZP-3mol% yttria-stabilized tetragonal zirconia poly crystal.
XRD	X-Ray-Diffraction
FE-SEM	Field-emission scanning electron microscopy
ROS	reactive oxygen species
PVA	Poly vinyl alcohol
CV	Crystal violet stain
LPS	lipopolysaccharides